JACS
JOURNAL OF THE AMERICAN CHEMICAL SOCIETY
pubs.acs.org/JACS
Article

Ordered–Disordered Ionic Cocrystalline Solid-State Electrolytes for Rapid Ion Migration in Sodium Metal Batteries

Binze Yang,[#] Xuan Liu,[#] Sheng Wen,[#] Zhihu You, Yizhi Xing, Shuzhang Ran, Pengbo Zhang, Jingyi Wang, Huan Li, Zuoxiu Tie, and Zhong Jin*

Cite This: J. Am. Chem. Soc. 2026, 148, 21588–21598

ABSTRACT: Solid-state electrolytes for sodium–metal batteries are restricted by intrinsically low ion mobility and stability. Herein, we report an ionic cocrystalline solid-state electrolyte featuring a unique ordered–disordered hybrid lattice by integrating sodium perchlorate with succinonitrile, namely, $NaClO_4(SN)_3$. It has a single phase with an ordered Na^+-coordination backbone, while orientationally disordered SN molecules reside in interstitial sites and serve as ionic pathways. This eutectic hybrid architecture establishes an ordered 3D continuous Na^+ single-ion conduction network associated with immobilized ClO_4^- anions, while supplemented by interconnected ionic flowpaths through disordered regions. This design principle enables rapid Na^+ hopping transport and maintains mechanical compliance for intimate electrode contact, thereby mitigating polarization and promoting uniform sodium deposition. The $NaClO_4(SN)_3$ electrolyte exhibits a low activation energy of 0.26 eV, an ionic conductivity of 0.94 mS cm^{-1} at 25 °C, and an electrochemical stability window beyond 4.6 V (vs Na/Na^+). It also features a melting point of 36.2 °C and a glass-transition temperature of −37.9 °C, allowing convenient *in situ* melting infiltration into electrodes followed by solidification to form conformal, low-impedance interfaces with enhanced dendrite resistance. These combined attributes exemplify an order–disorder hybrid cocrystal engineering strategy to develop solid-state electrolytes with rapid ionic conductivity, long cycling durability, and cost-effective scalability, providing a promising solution for rechargeable solid-state alkali metal batteries.

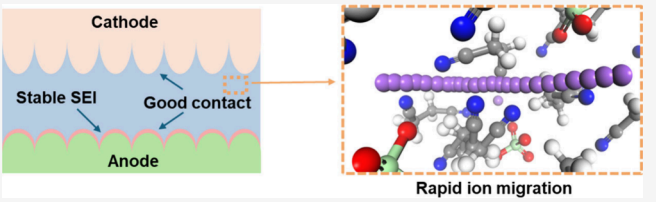

INTRODUCTION

Sodium metal batteries are promising candidates for large-scale energy storage, owing to the rich natural abundance and high theoretical capacity of sodium.[1−4] However, conventional organic liquid electrolytes for sodium metal batteries are flammable, which poses intrinsic safety risks in practical applications. Although a variety of inorganic, polymer, and composite solid-state electrolytes have been explored as alternatives,[5,6] many still suffer from limited Na^+ conductivity at ambient temperature, low transference number of Na^+, relatively narrow electrochemical stability windows, and/or inadequate interfacial stability. Fully inorganic solid-state electrolytes can deliver Na^+ conductivities on the order of 10^{-3} S cm^{-1},[7−12] but they typically suffer from high grain-boundary resistance and require externally applied stack pressure to maintain stable ionic conduction. Polymer electrolytes have been extensively explored because of the flexibility and ease of processing,[13−20] yet they generally exhibit room-temperature Na^+ conductivities below 10^{-4} S cm^{-1}. Composite electrolytes comprising polymer matrices and ceramic fillers leverage the high ionic conduction and mechanical robustness,[21−26] but high filler loadings may induce mechanical brittleness and poor interfacial contact. Against these backdrops, it is necessary to design new phase structures and ion-transport mechanisms for realizing high-performance solid-state electrolytes.

Herein, we present the design of an ionic cocrystalline electrolyte featuring a unique ordered–disordered hybrid lattice composed of sodium perchlorate ($NaClO_4$) and succinonitrile (SN), denoted as $NaClO_4(SN)_3$. Specifically, $NaClO_4$ and $NaClO_4$ and two-thirds of SN molecules cocrystallize into a single phase featuring an ordered ionic backbone where Na^+ occupies octahedral sites coordinated by two O atoms in ClO_4^- and four N atoms in SN, while additional SN molecules reside in interstitial sites with orientational disorder and serve as ionic flowpaths. This hybrid architecture establishes a continuous 3D Na^+ transport network while immobilizing ClO_4^- anions, thereby enabling effective single-ion conduction and maintaining mechanical compliance for intimate electrode contact. *Ab initio* molecular dynamics simulations and experimental characterizations consistently demonstrate rapid Na^+ migration along vertex-

Received: January 19, 2026
Revised: May 7, 2026
Accepted: May 12, 2026
Published: May 22, 2026

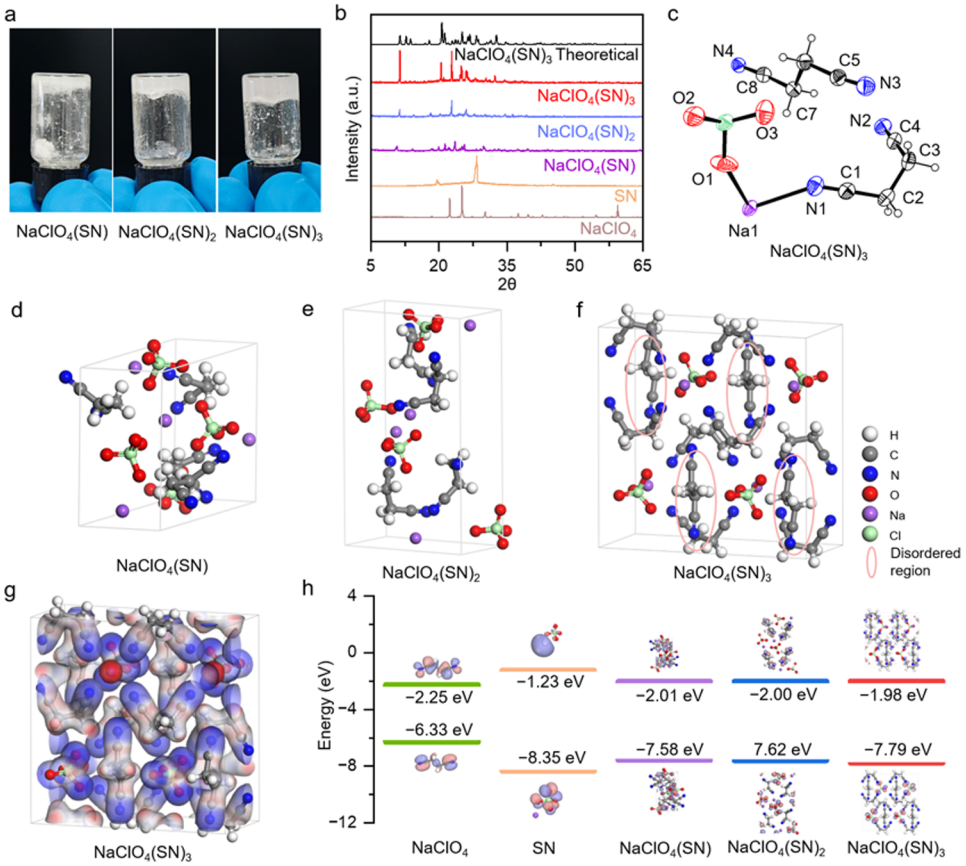

Figure 1. (a) Optical photographs of $NaClO_4(SN)$, $NaClO_4(SN)_2$, and $NaClO_4(SN)_3$ cocrystal electrolytes. (b) Theoretical (top) and experimental XRD patterns of different samples. (c) ORTEP representation of single-crystal $NaClO_4(SN)_3$. (d–f) Single-crystal structures of (d) $NaClO_4(SN)$, (e) $NaClO_4(SN)_2$, and (f) $NaClO_4(SN)_3$ cocrystal electrolytes. (g) ESP mapping of $NaClO_4(SN)_3$. (h) Calculated HOMO–LUMO energy levels of different samples.

to-vertex channels within the ordered sublattice, supplemented by interconnected ionic pathways through disordered regions. Immobilization of ClO_4^- anions in the ordered sublattice yields single-ion conduction, mitigating polarization and promoting uniform sodium deposition. This "ordered Na^+-coordination backbone plus disordered ionic flowpaths" design principle plays a pivotal role in constructing stable ion-conducting frameworks and facilitating rapid Na^+ hopping transport. Benefiting from its interconnected ion-conducting channels, the as-prepared $NaClO_4(SN)_3$ cocrystal electrolyte delivers a low activation energy of 0.26 eV and an exceptional Na^+ ionic conductivity of 0.94 S cm^{-1} at 25 °C, together with an electrochemical stability window beyond 4.6 V (vs Na/Na^+). Moreover, the $NaClO_4(SN)_3$ cocrystal electrolyte features a melting point of 36.2 °C and a glass-transition temperature of − 37.9 °C, allowing *in situ* melting infiltration into electrodes followed by solidification to form conformal, low-impedance interfaces with enhanced dendrite resistance. Additionally, the $NaClO_4(SN)_3$ cocrystalline electrolyte integrates facile processing characteristics and cost-effective scalability, rendering it suitable for practical deployment. In symmetric Na||Na batteries, the $NaClO_4(SN)_3$ cocrystal electrolyte supports a critical current density of 10.0 mA cm^{-2} and enables stable plating/stripping for over 1300 h at 2.0 mAh cm^{-2} and 1.0 mA cm^{-2} with an overpotential of ∼35 mV, while the interfacial impedance is as low as 220.78 Ω·cm^2. In $Na_2Fe_2(SO_4)_3$||Na batteries, the $NaClO_4(SN)_3$ cocrystal electrolyte affords high-rate and long-life operation, retaining 83.9 mAh g^{-1} (89.6% capacity retention) after 300 cycles at 0.2 C and 69.16 mAh g^{-1} (84.9% retention) after 1500 cycles at 0.5 C, with a median discharge voltage above 3.53 V. This study offers an ordered–disordered ionic cocrystal strategy to develop solid-state electrolytes that combine high ionic conductivity, dendrite-resistant interfaces, and long cycling durability for advanced alkali metal secondary batteries.

RESULTS AND DISCUSSION

To prepare the cocrystal solid-state electrolytes, the mixtures of $NaClO_4$ and SN in molar ratios of 1:1, 1:2, and 1:3 were melted and continuously stirred for 12 h at 60 °C to ensure complete dissolution and intimate mixing. Subsequently, the melts were cooled to room temperature to induce cocrystallization. The resulting solids, denoted $NaClO_4(SN)$, $NaClO_4(SN)_2$, and $NaClO_4(SN)_3$, respectively, appear as transparent or semitransparent blocks with slight differences in clarity and texture that reflect different nucleation and crystal-growth behaviors (Figure 1a). ClO_4^- is a highly symmetric tetrahedral oxoanion with four equivalent O-donor sites, enabling repeated Na–O coordination and a continuous Na^+ coordination network. Combined with SN, which also contributes Na^+–N interactions, this favors an extended cocrystalline framework with percolating Na^+ transport pathways, while the weakly coordinating nature of perchlorate stabilizes the lattice without strongly trapping Na^+. Powder X-ray diffraction (XRD) patterns of these samples (Figure 1b) show that the characteristic diffraction peaks of pristine

https://doi.org/10.1021/jacs.6c01095
J. Am. Chem. Soc. 2026, 148, 21588–21598

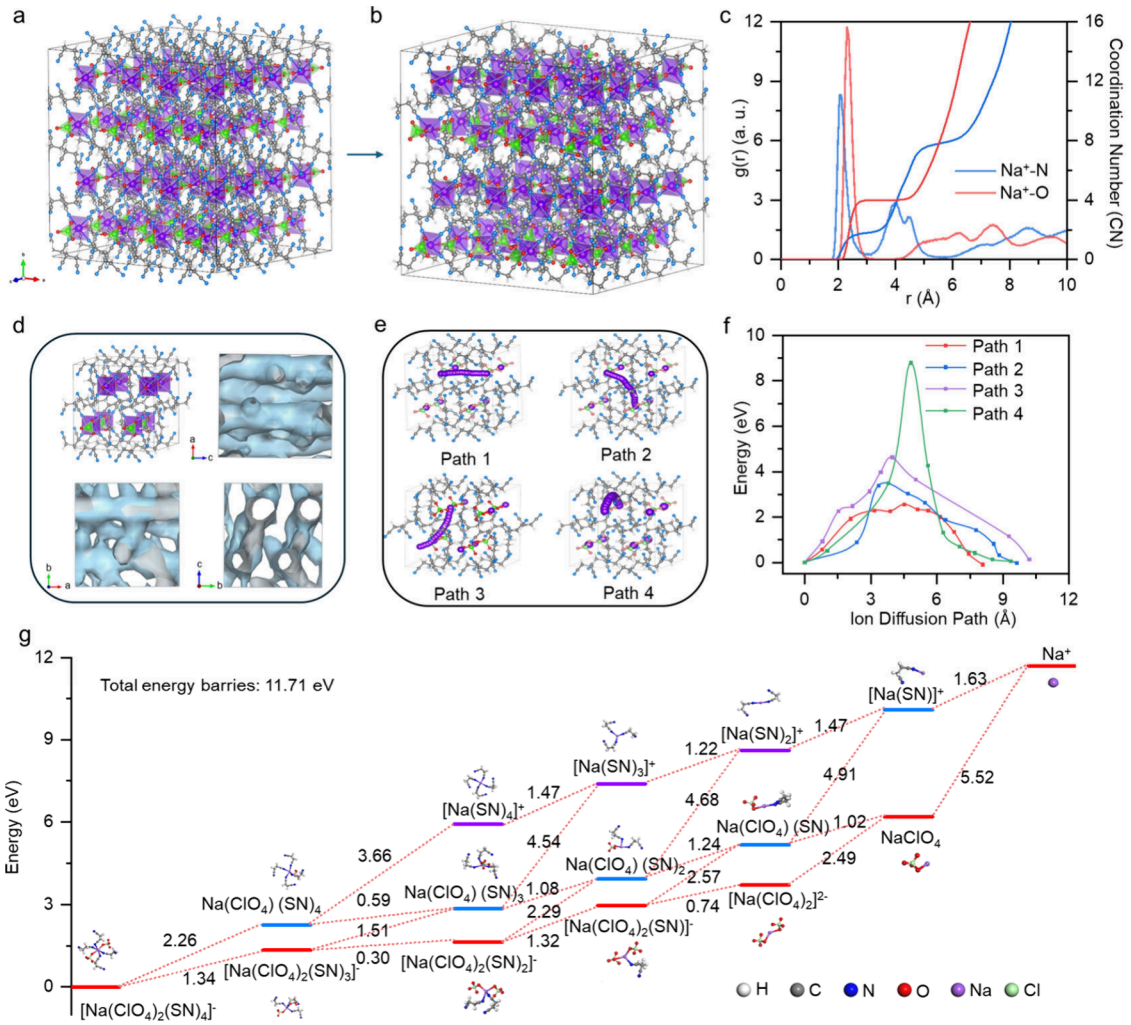

Figure 2. MD simulation snapshots of the $NaClO_4(SN)_3$ cocrystal electrolyte system (a) at the initial state and (b) after 50 ns at 298 K. (c) RDF and CN profiles for (blue) Na^+−N and (red) Na^+−O pairs obtained from MD simulations of $NaClO_4(SN)_3$. (d) 1 × 2 × 1 supercell crystal structure of $NaClO_4(SN)_3$ and 3D isosurface map of the accessible Na^+ migration regions obtained from AIMD simulations. (e) Schematic depiction of four representative Na^+ migration channels and (f) their corresponding Na^+ migration energy barriers in $NaClO_4(SN)_3$. (g) Diagram of the energy barriers for Na^+ migration out of the octahedral coordination sites within the $NaClO_4(SN)_3$ crystal (the blue text indicates that in this structure two oxygen atoms on one perchlorate anion are involved in coordination).

$NaClO_4$ and SN disappear, while new peaks emerge and intensify when the content of SN increases. For $NaClO_4(SN)_3$, the experimental XRD pattern matches well with that simulated from single-crystal data, confirming the formation of a highly crystalline, single-phase cocrystal structure. The detailed atomic arrangements of $NaClO_4(SN)$, $NaClO_4(SN)_2$, and $NaClO_4(SN)_3$ were resolved by single-crystal XRD and presented as Oak Ridge Thermal Ellipsoid Plot (ORTEP) representations in Figure 1c and Figure S1.[27−34] These high-resolution structural data are essential for obtaining clear phase identification and for understanding how local coordination geometry may influence ion transport pathways.[35] The single-crystal structure views of $NaClO_4(SN)$, $NaClO_4(SN)_2$, and $NaClO_4(SN)_3$ are illustrated in Figure 1d−1f, and their detailed single-crystal data and unit-cell parameters are provided Tables S1−S18. For $NaClO_4(SN)$ and $NaClO_4(SN)_2$ cocrystals, they share essentially the same local coordination environment, in which each Na^+ center adopts a 5-fold coordination geometry involving three ClO_4^- anions and two SN molecules. Specifically, for $NaClO_4(SN)_3$, $NaClO_4$ and two-thirds of the SN molecules cocrystallize into a single phase featuring an ordered ionic backbone where Na^+ occupies octahedral sites coordinated by two O atoms in ClO_4^- and four N atoms in SN, while the remaining SN molecules reside in interstitial sites with orientational disorder and serve as ionic flowpaths.

Density functional theory (DFT) calculations were conducted to reveal the electronic structures of the samples.[36−39] The electrostatic potential (ESP) mappings of $NaClO_4$ and SN precursors were displayed in Figure S2. The combination of ordered Na^+ coordination polyhedra and locally disordered SN units is further illustrated by the ESP mapping in Figure 1g, which highlights electron-rich nitrile (−C≡N) of SN and carbonyl (−C═O) of ClO_4^- with strong affinity to Na^+. The coexistence of a rigid, high-symmetry conduction scaffold of ordered Na^+-coordination backbone and disordered SN molecule domains is expected to preserve a low-energy ion migration barrier and introduce auxiliary Na^+ hopping channels. Frontier-orbital calculations for $NaClO_4$, SN, $NaClO_4(SN)$, $NaClO_4(SN)_2$, and $NaClO_4(SN)_3$ (Figure 1h) show that the highest occupied molecular orbital (HOMO) levels of the cocrystalline electrolytes are progressively lowered

https://doi.org/10.1021/jacs.6c01095
J. Am. Chem. Soc. 2026, 148, 21588−21598

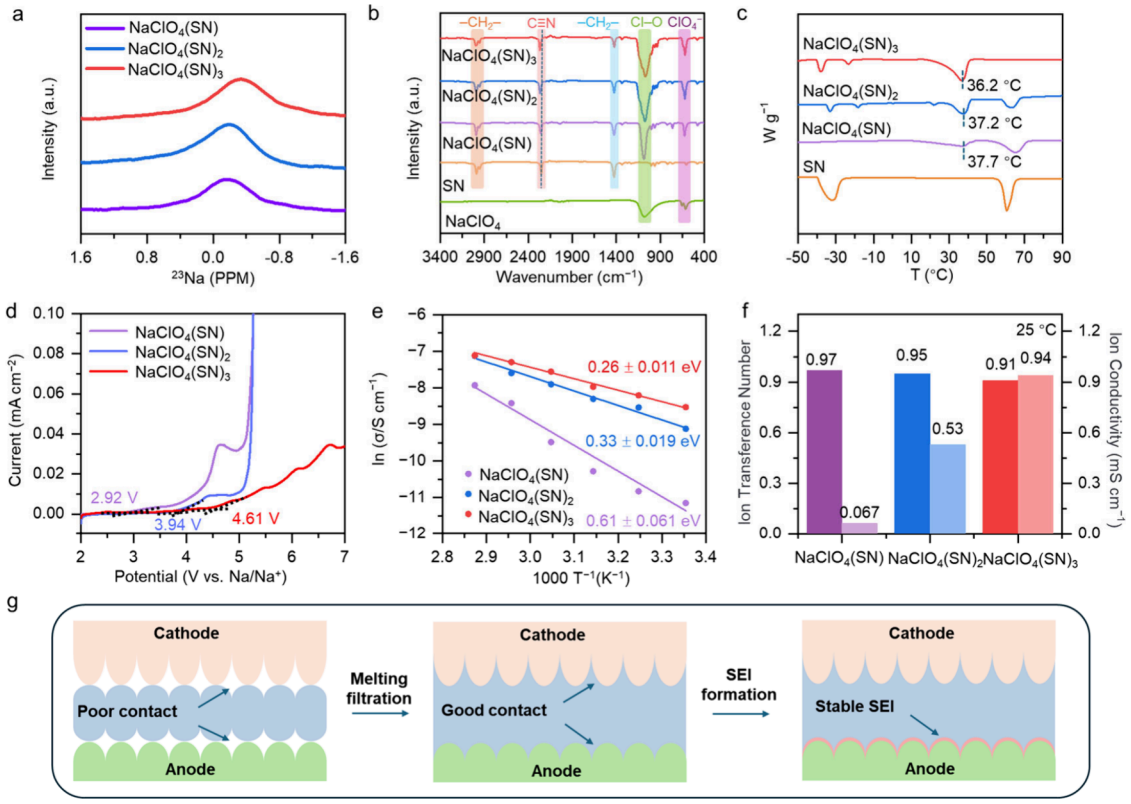

Figure 3. (a) ^{23}Na NMR spectra showing the chemical shifts induced by Na^+ coordination. (b) FTIR spectra revealing the chemical shifts of C≡N groups and perchlorate anions upon coordination. (c) DSC curves characterizing the melting points and the glass transition temperatures of the samples. (d) LSV curves for determining the electrochemical stability windows of the samples. (e) Ion migration energy barriers obtained by fitting the Arrhenius equation. (f) Room-temperature Na^+ ionic conductivities and ionic transference numbers of the samples. (g) Schematic illustration of the *in situ* melting filtration and SEI formation processes.

relative to pristine $NaClO_4$ as the SN content increases, while the lowest unoccupied molecular orbital (LUMO) levels remain close to that of $NaClO_4$. The deeper HOMO level suggests a reduced intrinsic tendency toward anodic oxidation,[40] which is qualitatively consistent with the improved anodic stability experimentally observed for $NaClO_4(SN)_3$. As a result, the cocrystals exhibit larger HOMO−LUMO gaps than pristine $NaClO_4$, suggesting reduced electronic reactivity of the $NaClO_4$-derived states within the SN matrix.

Molecular dynamics (MD) simulations were performed to provide atomistic insight into the structure characteristics of the $NaClO_4(SN)_3$ cocrystal electrolyte system.[41−46] The MD snapshots in Figure 2a and 2b confirm that, after equilibration at 298 K, the lattice of the $NaClO_4(SN)_3$ cocrystal preserves long-range order. Radial distribution functions (RDF) and coordination number (CN) profile analyses are shown in Figure 2c. The calculated CN is 4 (for Na^+−N) and 2 (for Na^+−O), defining a pseudo-octahedral first shell. The $Na[N]_4[O]_2$ octahedra and $Cl[O]_4$ tetrahedra feature an ordered ionic coordination backbone while additional SN molecules reside in interstitial sites, thereby maintaining the intended ordered−disordered hybrid framework. The mixed N/O coordination rationalizes selective transport of Na^+ in the immobilized, rigid anion framework and provides a structurally symmetric cage from which Na^+ hopping transport can be initiated.

Ab initio molecular dynamics (AIMD) simulations (Figure 2d and Figure S3) reveal the Na^+ diffusion isosurfaces in blue mesh maps, presenting the three-dimensional network of accessible pathways within the cocrystal lattice of $NaClO_4(SN)_3$. Collectively, observations along the a, b, and c crystallographic axes show that these ordered and disordered ionic pathways form an interconnect network with necessary redundancy and enhanced robustness. This network comprises well-defined octahedral-vertex-vertex channels that ensure directional low-impedance ion transport, while additional disordered ionic flowpaths created by SN side-chains lead to conformational disorder and local ClO_4^- perturbations. The energy barrier profiles for four representative Na^+ diffusion paths are drawn in Figure 2e and quantified in Figure 2f. Path 1, which traverses directly between adjacent octahedral vertices, requires only 2.55 eV and thus serves as the primary high-effective conduction route. Path 2 and Path 3, which partially traverse the disordered regions, exhibit moderate energy barriers of 3.39 and 4.63 eV, respectively, indicating that the local disorder does not hinder but rather supplements the main conduction channel by offering alternative ionic hopping sites. In contrast, Path 4, although following an equally long and tortuous migration trajectory, completely bypasses the disordered regions and therefore encounters a substantially higher barrier (8.78 eV). This result underscores that Na^+ migration in a purely ordered environment is energetically costly, whereas rational incorporation of disordered segments into the ordered backbone helps enhance ionic conduction efficiency. These findings suggest that the "ordered Na^+-coordination backbone plus disordered ionic flowpaths" motif in $NaClO_4(SN)_3$ strikes an optimal balance between low-energy, high-symmetry conduction routes and

https://doi.org/10.1021/jacs.6c01095
J. Am. Chem. Soc. 2026, 148, 21588−21598

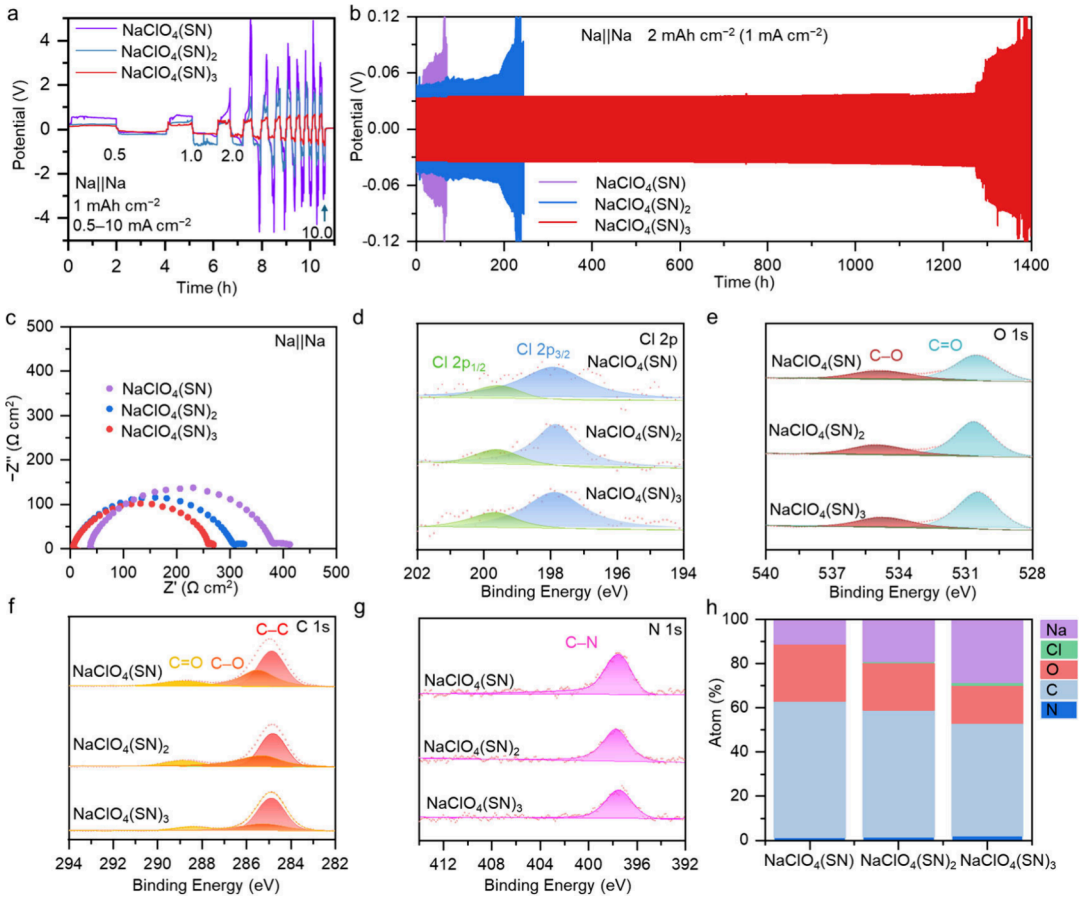

Figure 4. (a) Voltage responses during critical current density measurements of Na||Na symmetric batteries based on various electrolytes (1.0 mAh cm^{-2}, 0.5−10.0 mA cm^{-2}). (b) Galvanostatic cycling of Na||Na symmetric batteries at 2.0 mAh cm^{-2} and 1.0 mA cm^{-2}. (c) EIS analyses of Na||Na symmetric batteries. (d) Cl 2p, (e) O 1s, (f) C 1s, and (g) N 1s XPS spectra and (h) corresponding elemental compositions of the SEI layers formed by different cocrystal electrolytes in Na||Na symmetric batteries after galvanostatic cycling for 1300 h.

auxiliary pathways that kick in when the primary channel is transiently blocked.

Ion decoordination is also a crucial step in the overall ion transport process.[47,48] Figure 2g presents the stepwise energy profiles for Na^+ decoordination from the $NaClO_4(SN)_3$ lattice via a competitive coordination mechanism, with a total energy barrier of 11.71 eV, higher than that of 9.6 eV obtained for $NaClO_4(SN)_2$ and $NaClO_4(SN)$ (Figure S4), indicating more enhanced delocalization of Na^+ in $NaClO_4(SN)_3$. As Na^+ moves away from its original pseudo-octahedral coordination site, each rise in the energy curve corresponds to a discrete leaving ligand event until Na^+ is completely released from its coordination cage. These energy barriers collectively define the interfacial decoordination threshold, which is distinct from the site-to-site migration barriers within the bulk electrolyte. It reveals that solid-state Na^+ transport in $NaClO_4(SN)_3$ is finely regulated by decoordination processes, providing a theoretical basis for ion transfer across the electrode−electrolyte interface.

To assess the structure−property relationships of the cocrystalline electrolytes, a combination of spectroscopic, thermal, and electrochemical measurements was performed. To elucidate the local coordination environment that underpins rapid ion transport, ^{23}Na nuclear magnetic resonance (NMR) spectroscopy was conducted (Figure 3a), as ^{23}Na chemical shifts are strongly dependent on the Na^+ coordination environment including the ligand identity and Na−donor distances.[49] The ^{23}Na chemical-shift trends are consistent with increased involvement of nitrile-N donors in the Na^+ coordination, as identified by single-crystal XRD analyses. The Fourier transform infrared spectroscopy (FTIR) spectra in Figure 3b (together with Raman spectra in Figure S5) display a shift of the C≡N stretching band from 2252.45 cm^{-1} to 2262.88 cm^{-1} and the changes in the Cl−O band near 1074.16 cm^{-1}, respectively. These results directly evidence Na^+−SN and Na^+−ClO_4^- interactions that construct ordered/disordered hybrid conduction pathways and reflect the enhanced delocalization of Na^+ ions. Differential scanning calorimetry (DSC) shows that $NaClO_4(SN)_3$ melts at 36.2 °C and undergoes vitrification at −37.9 °C, while the melting point increases to 44.1 °C after melt infiltration into a glass-fiber separator (Figure 3c and Figure S6), thereby providing a wide processing window for *in situ* molten infiltration and subsequent solidification.

The electrochemical stability of the cocrystal electrolytes was evaluated by linear sweep voltammetry (LSV) on Na|electrolyte|stainless steel batteries. As shown in Figure 3d and Figure S7, $NaClO_4(SN)_3$ exhibits an antioxidation cutoff potential beyond 4.61 V versus Na/Na^+ and an antireduction cutoff potential of 1.24 V versus Na/Na^+, indicating a broad electrochemical stability window that is sufficient for the application in high-voltage Na-ion batteries.[50,51] The Arrhenius fittings of the ionic conductivity data (Figure 3e and Figure S8) yield an activation energy of only 0.26 eV for $NaClO_4(SN)_3$, much lower than those of $NaClO_4(SN)$ (0.61

https://doi.org/10.1021/jacs.6c01095
J. Am. Chem. Soc. 2026, 148, 21588−21598

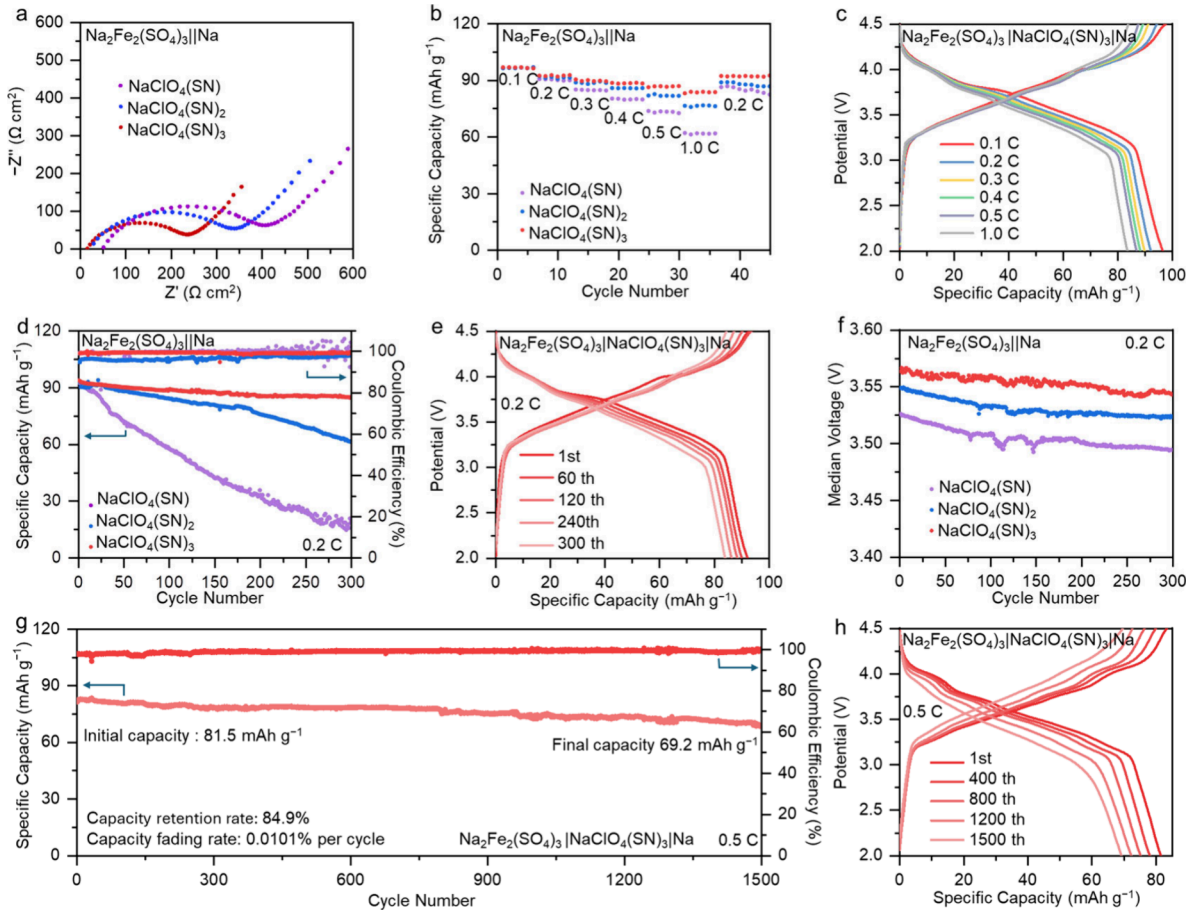

Figure 5. (a) EIS analyses of $Na_2Fe_2(SO_4)_3$||Na batteries with different cocrystal electrolytes. (b) Rate capabilities and (c) corresponding charge−discharge curves of $Na_2Fe_2(SO_4)_3$||Na batteries from 0.1 to 1.0 C. (d) Cycling performances of $Na_2Fe_2(SO_4)_3$||Na batteries at 0.2 C. (e) Charge−discharge curves of $Na_2Fe_2(SO_4)_3$|$NaClO_4(SN)_3$|Na batteries with a $NaClO_4(SN)_3$ electrolyte at 0.2 C. (f) Median voltage evolutions during cycling of $Na_2Fe_2(SO_4)_3$||Na batteries with $NaClO_4(SN)$, $NaClO_4(SN)_2$, and $NaClO_4(SN)_3$ electrolytes, respectively. (g) Long-term cycling performances and (h) corresponding charge−discharge curves of $Na_2Fe_2(SO_4)_3$|$NaClO_4(SN)_3$|Na batteries at 0.5 C.

eV) and $NaClO_4(SN)_2$ (0.34 eV), underscoring facile Na^+ hopping within the hybrid architecture framework of $NaClO_4(SN)_3$.[52] $NaClO_4(SN)_3$ shows a smooth σ−T increase without a step change near the nominal melting point. This behavior is consistent with SN-derived plastic-crystal/soft ion cocrystalline electrolytes,[35,46] in which orientational disorder and defect-assisted ion transport develop progressively with temperature. Temperature-dependent electrochemical impedance spectroscopy (EIS) analyses (Figure S9) show that the impedance of $NaClO_4(SN)_3$ rises steeply at 0 °C and increases by about 2 orders of magnitude between −20 and −30 °C, consistent with SN approaching its glass transition temperature, where the SN molecule orientations freeze and the coupled Na^+ hopping pathways collapse, thus hampering low-temperature ionic transport. As summarized in Figure 3f and Figure S10, $NaClO_4(SN)_3$ delivers an exceptional Na^+ conductivity of 0.94 mS cm^{-1} at 25 °C. The Na^+ transference numbers of $NaClO_4(SN)$, $NaClO_4(SN)_2$, and $NaClO_4(SN)_3$ reach 0.97, 0.95, and 0.94, respectively, indicating that the charge transport is dominated by Na^+ and the immobilization of ClO_4^- anions enables effective single-ion conduction. Electronic leakage in solid-state electrolytes may promote continuous dendritic deposition within the electrolyte and ultimately facilitate the formation of percolating metallic filaments, thereby increasing the likelihood of internal short circuits.[53] In this work, the electronic conductivities of $NaClO_4(SN)$, $NaClO_4(SN)_2$, and $NaClO_4(SN)_3$ are estimated to be 7.98×10^{-11}, 1.40×10^{-10}, and 1.90×10^{-10} S·cm^{-1}, respectively (Figure S11). These low electronic conductivities indicate an electronically insulating nature, which is beneficial to suppressing electron-penetration-induced parasitic reactions and thereby mitigating the risks of internal short-circuits and self-discharge. Atomic force microscopy (AFM) force−indentation measurements were conducted to quantify the effective Young's modulus of $NaClO_4(SN)_x$. The extracted moduli are 26.4 kPa for $NaClO_4(SN)$, 12.8 kPa for $NaClO_4(SN)_2$, and 17.9 kPa for $NaClO_4(SN)_3$ in Figure S12. These values confirm that $NaClO_4(SN)_x$ is a very soft solid material with limited self-supporting capability. A glass-fiber separator was incorporated into the cell architecture to prevent internal short-circuiting between the cathode and anode during the *in situ* melting infiltration.[46] After battery assembly, $NaClO_4(SN)_3$ was melt-infiltrated and physically confined at the interface of the electrode and glass-fiber separator, which provided a mechanically robust scaffold and capillary confinement, helping maintain electrode/electrolyte contact and preventing internal short-circuiting. When the battery is operated at elevated temperatures above the melting point, $NaClO_4(SN)_3$ melts and forms a conventional eutectic electrolyte, enabling continued normal cell operation. The

https://doi.org/10.1021/jacs.6c01095
J. Am. Chem. Soc. 2026, 148, 21588−21598

schematic illustration in Figure 3g depicts the *in situ* melting infiltration and solid-electrolyte interphase (SEI) formation processes in $NaClO_4(SN)_3$ cocrystal electrolyte based batteries, in which mild heating allows $NaClO_4(SN)_3$ to melt and infiltrate into the nanopores of electrodes, followed by solidification into seamless, conformal interfaces and then forming a stable SEI coating layer during cycling, thereby minimizing interfacial resistance and enhancing cycling stability.

To evaluate the capability of cocrystal electrolytes for suppressing sodium dendrite formation under demanding plating/stripping conditions, the critical current density measurements were conducted.[54] As shown in Figure 4a, the Na||Na symmetric batteries with a $NaClO_4(SN)_3$ electrolyte cycled at 1.0 mAh cm^{-2} sustain a critical current density of 10.0 mA cm^{-2}. This indicates the formation of a robust interphase that resists uneven Na deposition and promotes uniform ion transport, which are key requirements for stable sodium metal anode operation. The long-term stability for Na plating/stripping was examined at a practical areal capacity of 2.0 mAh cm^{-2} under a current density of 1.0 mA cm^{-2}. The symmetric batteries with a $NaClO_4(SN)_3$ electrolyte continuously cycled for 1300 h with an overpotential of only 35.2 mV (Figure 4b). Such low polarization and high stability over extended cycling suggests that $NaClO_4(SN)_3$ maintains a highly conductive, mechanically stable interface. EIS analyses (Figure 4c) further reveal two distinct semicircles in the Nyquist plots, assigned to the SEI resistance (at the midfrequency region). Among the three electrolytes, $NaClO_4(SN)_3$ exhibits the lowest total interfacial resistance, signifying tighter physical contact and reduced space charge accumulation at the Na and electrolyte interface.

To clarify the chemical nature and origin of the SEI layer that underpins this electrochemical stability, X-ray photoelectron spectroscopy (XPS) was conducted on cycled Na electrodes and the pristine cocrystal electrolyte (Figure S13). The Cl 2p spectrum (Figure 4d) shows only Cl $2p_{3/2}$ (197.8 eV) and Cl $2p_{1/2}$ (200.1 eV) spin−orbit peaks, demonstrating that ClO_4^- remains electrochemically inert and contributes to interphase stability.[55−57] The O 1s signal at 531.0 eV (Figure 4e) further corroborates the presence of organic carbonates within the SEI. The C 1s spectrum (Figure 4f) displays dominant peaks at 284.8 eV (C−C), 286.2 eV (C−O), and 288.8 eV (C═O), indicating carbonate-rich organic components derived from partial SN decomposition, while the N 1s peak at 399.5 eV (Figure 4g and Figure S14) suggests that some of the nitrile groups in SN remain intact and coordinate with Na^+ to help form continuous conducting channels. The corresponding elemental compositions shown in Figure 4h, presented as semiquantitative, trend-based comparisons under identical acquisition and fitting conditions, reflect an organic-rich SEI layer enriched in C, Na, and O with minor N and Cl components. Such ion-conductive yet electronically insulating SEI components promote interfacial passivation, thereby establishing a Na-rich interphase that facilitates Na^+ transport and supports long-term cycling stability.

The Nyquist plots in Figure 5a verify that $Na_2Fe_2(SO_4)_3$|$NaClO_4(SN)_3$|Na batteries exhibit the lowest interfacial impedance of 220.78 $\Omega\cdot cm^2$ compared to those of $NaClO_4(SN)$ and $NaClO_4(SN)_2$ counterparts. Such low impedance benefits from its low melting point and *in situ* solidification, which together ensure intimate interfacial contact with both the electrodes and minimize space charge accumulation at the interfaces. By utilizing a $NaClO_4(SN)_3$ electrolyte, the high-voltage $Na_2Fe_2(SO_4)_3$ cathode (Figure 5b) delivers the highest specific capacities, maintaining 96.7, 91.9, 89.5, 88.2, 86.3, and 83.0 mAh g^{-1} at 0.1, 0.2, 0.3, 0.4, 0.5, and 1.0 C, respectively. This impressive rate performance is attributed to its high Na^+ conductivity, which originates from the stable ion-conducting framework and rapid Na^+ hopping transport in the $NaClO_4(SN)_3$ electrolyte. The nearly overlapping charge−discharge profiles of $Na_2Fe_2(SO_4)_3$|$NaClO_4(SN)_3$|Na batteries in Figure 5c demonstrate negligible polarization even at high current rates, indicating uniform Na^+ transport and preventing local charge buildup.

Relying on the $NaClO_4(SN)_3$ electrolyte, the $Na_2Fe_2(SO_4)_3$||Na batteries retain a specific capacity of 83.9 mAh g^{-1} (corresponding to a capacity retention of 89.6%) after 300 cycles at 0.2 C, reflecting robust cathode−electrolyte compatibility (Figure 5d). The nearly identical charge−discharge curves in Figure 5e confirm minimal structural or interfacial degradation supported by the $NaClO_4(SN)_3$ electrolyte. Figure 5f illustrates that the median discharge voltage of $NaClO_4(SN)_3$-based batteries remains above 3.53 V, evidencing low polarization and high stability of SEI over cycling. During long-term charge−discharge cycling at 0.5 C (Figure 5g), the $Na_2Fe_2(SO_4)_3$|$NaClO_4(SN)_3$|Na batteries maintain a specific capacity of 69.16 mAh g^{-1} after 1500 cycles, corresponding to a capacity retention of 84.9% and demonstrating exceptional endurance under rigorous conditions. The superimposed profiles before and after long-term cycling in Figure 5h reveal virtually unchanged polarization and low impedance, underscoring the integrity of electrode−electrolyte interfaces.

The low-temperature durability of cocrystal electrolytes was further evaluated (Figure S15). The $Na_2Fe_2(SO_4)_3$||Na batteries with a $NaClO_4(SN)_3$ electrolyte sustain a specific capacity of 75.8 mAh g^{-1} at 0 °C, while the $NaClO_4(SN)$ and $NaClO_4(SN)_2$ counterparts deliver 10.7 and 65.8 mAh g^{-1}, respectively. The low-temperature operability of $NaClO_4(SN)_3$ is attributed to its ordered−disordered cocrystal architecture in which orientationally disordered SN units maintain rotational dynamics and provide auxiliary ionic pathways that couple molecular reorientation to ion transport. The relatively wide electrochemical stability window of $NaClO_4(SN)_3$ enables its compatibility with diverse cathode chemistries. As a representative example, the $NaFe_{0.3}Ni_{0.3}Mn_{0.3}O_2$|$NaClO_4(SN)_3$|Na batteries deliver an initial specific capacity of 125.60 mAh g^{-1} and retain 120.63 mAh g^{-1} after 100 cycles at 0.5 C, corresponding to a capacity retention of 96.0%, confirming the applicability of this cocrystal electrolyte to high-voltage layered oxide cathode materials (Figure S16). As summarized in Table S19, the $NaClO_4(SN)_3$ cocrystal electrolyte achieves a well-balanced optimization of room-temperature ionic conductivity, Na^+ transference number, and long-term cycling stability, which compares favorably with representative solid-state electrolytes for sodium metal batteries.

CONCLUSION

In summary, we present the design of a $NaClO_4(SN)_3$ ionic cocrystalline electrolyte assembled by an ordered Na^+-coordination backbone and orientationally disordered SN molecules as the peripheral auxiliary component. This architecture constructs a continuous 3D Na^+ transport network with immobilized ClO_4^- anions, enabling effective single-ion

https://doi.org/10.1021/jacs.6c01095
J. Am. Chem. Soc. 2026, 148, 21588−21598

conduction and maintaining mechanical compliance for intimate electrode contact. *Ab initio* molecular dynamics simulations and experimental characterizations consistently support this "ordered Na^+-coordination backbone plus disordered ionic flowpaths" design principle and clarify its pivotal role in constructing stable ion-conducting frameworks and facilitating rapid Na^+ hopping transport. Benefiting from its interconnected ion-conducting channels, $NaClO_4(SN)_3$ delivers a low activation energy of 0.26 eV and a high Na^+ ionic conductivity of 0.94 mS cm^{-1} at 25 °C. In full batteries paired with high-voltage $Na_2Fe_2(SO_4)_3$ cathodes, the $NaClO_4(SN)_3$ electrolyte supports favorable interfacial ion conduction and sustained high-voltage output over prolonged cycling, demonstrating impressive long-term durability. Moreover, the cocrystalline electrolyte integrates these electrochemical advantages with facile processing and cost-effective scalability, indicating promise for practical deployment. These combined attributes exemplify an order−disorder hybrid cocrystal engineering strategy to develop solid-state electrolytes with rapid ionic conductivity and long cycling durability, providing a promising solution for rechargeable solid-state alkali metal batteries.

■ ASSOCIATED CONTENT

Supporting Information

The Supporting Information is available free of charge at https://pubs.acs.org/doi/10.1021/jacs.6c01095.

Experimental section (including material preparation, material characterizations, electrochemical measurements, and theoretical calculations), additional figures (Figures S1−S16), additional tables (Tables S1−S19) (PDF)

Accession Codes

Deposition Numbers 2410574, 2414830, and 2472878 contain the supplementary crystallographic data for this paper. These data can be obtained free of charge via the joint Cambridge Crystallographic Data Centre (CCDC) and Fachinformationszentrum Karlsruhe Access Structures service.

■ AUTHOR INFORMATION

Corresponding Author

Zhong Jin − *State Key Laboratory of Coordination Chemistry, MOE Key Laboratory of Mesoscopic Chemistry, MOE Key Laboratory of High Performance Polymer Materials and Technology, Jiangsu Key Laboratory of Green Energy Catalysis and Intelligent Chemical Engineering, Suzhou Key Laboratory of Green Intelligent Manufacturing of New Energy Materials and Devices, Tianchang New Materials and Energy Technologies Research Center, Institute of Green Chemistry and Engineering, School of Chemistry and Chemical Engineering, Nanjing University, Nanjing, Jiangsu 210023, P. R. China*; orcid.org/0000-0001-8860-8579; Email: zhongjin@nju.edu.cn

Authors

Binze Yang − *State Key Laboratory of Coordination Chemistry, MOE Key Laboratory of Mesoscopic Chemistry, MOE Key Laboratory of High Performance Polymer Materials and Technology, Jiangsu Key Laboratory of Green Energy Catalysis and Intelligent Chemical Engineering, Suzhou Key Laboratory of Green Intelligent Manufacturing of New Energy Materials and Devices, Tianchang New Materials and Energy Technologies Research Center, Institute of Green Chemistry and Engineering, School of Chemistry and Chemical Engineering, Nanjing University, Nanjing, Jiangsu 210023, P. R. China*

Xuan Liu − *State Key Laboratory of Coordination Chemistry, MOE Key Laboratory of Mesoscopic Chemistry, MOE Key Laboratory of High Performance Polymer Materials and Technology, Jiangsu Key Laboratory of Green Energy Catalysis and Intelligent Chemical Engineering, Suzhou Key Laboratory of Green Intelligent Manufacturing of New Energy Materials and Devices, Tianchang New Materials and Energy Technologies Research Center, Institute of Green Chemistry and Engineering, School of Chemistry and Chemical Engineering, Nanjing University, Nanjing, Jiangsu 210023, P. R. China*

Sheng Wen − *State Key Laboratory of Coordination Chemistry, MOE Key Laboratory of Mesoscopic Chemistry, MOE Key Laboratory of High Performance Polymer Materials and Technology, Jiangsu Key Laboratory of Green Energy Catalysis and Intelligent Chemical Engineering, Suzhou Key Laboratory of Green Intelligent Manufacturing of New Energy Materials and Devices, Tianchang New Materials and Energy Technologies Research Center, Institute of Green Chemistry and Engineering, School of Chemistry and Chemical Engineering, Nanjing University, Nanjing, Jiangsu 210023, P. R. China*

Zhihu You − *State Key Laboratory of Coordination Chemistry, MOE Key Laboratory of Mesoscopic Chemistry, MOE Key Laboratory of High Performance Polymer Materials and Technology, Jiangsu Key Laboratory of Green Energy Catalysis and Intelligent Chemical Engineering, Suzhou Key Laboratory of Green Intelligent Manufacturing of New Energy Materials and Devices, Tianchang New Materials and Energy Technologies Research Center, Institute of Green Chemistry and Engineering, School of Chemistry and Chemical Engineering, Nanjing University, Nanjing, Jiangsu 210023, P. R. China*

Yizhi Xing − *State Key Laboratory of Coordination Chemistry, MOE Key Laboratory of Mesoscopic Chemistry, MOE Key Laboratory of High Performance Polymer Materials and Technology, Jiangsu Key Laboratory of Green Energy Catalysis and Intelligent Chemical Engineering, Suzhou Key Laboratory of Green Intelligent Manufacturing of New Energy Materials and Devices, Tianchang New Materials and Energy Technologies Research Center, Institute of Green Chemistry and Engineering, School of Chemistry and Chemical Engineering, Nanjing University, Nanjing, Jiangsu 210023, P. R. China*

Shuzhang Ran − *State Key Laboratory of Coordination Chemistry, MOE Key Laboratory of Mesoscopic Chemistry, MOE Key Laboratory of High Performance Polymer Materials and Technology, Jiangsu Key Laboratory of Green Energy Catalysis and Intelligent Chemical Engineering, Suzhou Key Laboratory of Green Intelligent Manufacturing of New Energy Materials and Devices, Tianchang New Materials and Energy Technologies Research Center, Institute of Green Chemistry and Engineering, School of Chemistry and Chemical Engineering, Nanjing University, Nanjing, Jiangsu 210023, P. R. China*

Pengbo Zhang − *State Key Laboratory of Coordination Chemistry, MOE Key Laboratory of Mesoscopic Chemistry, MOE Key Laboratory of High Performance Polymer*

Materials and Technology, Jiangsu Key Laboratory of Green Energy Catalysis and Intelligent Chemical Engineering, Suzhou Key Laboratory of Green Intelligent Manufacturing of New Energy Materials and Devices, Tianchang New Materials and Energy Technologies Research Center, Institute of Green Chemistry and Engineering, School of Chemistry and Chemical Engineering, Nanjing University, Nanjing, Jiangsu 210023, P. R. China

Jingyi Wang − *State Key Laboratory of Coordination Chemistry, MOE Key Laboratory of Mesoscopic Chemistry, MOE Key Laboratory of High Performance Polymer Materials and Technology, Jiangsu Key Laboratory of Green Energy Catalysis and Intelligent Chemical Engineering, Suzhou Key Laboratory of Green Intelligent Manufacturing of New Energy Materials and Devices, Tianchang New Materials and Energy Technologies Research Center, Institute of Green Chemistry and Engineering, School of Chemistry and Chemical Engineering, Nanjing University, Nanjing, Jiangsu 210023, P. R. China*

Huan Li − *State Key Laboratory of Coordination Chemistry, MOE Key Laboratory of Mesoscopic Chemistry, MOE Key Laboratory of High Performance Polymer Materials and Technology, Jiangsu Key Laboratory of Green Energy Catalysis and Intelligent Chemical Engineering, Suzhou Key Laboratory of Green Intelligent Manufacturing of New Energy Materials and Devices, Tianchang New Materials and Energy Technologies Research Center, Institute of Green Chemistry and Engineering, School of Chemistry and Chemical Engineering, Nanjing University, Nanjing, Jiangsu 210023, P. R. China*

Zuoxiu Tie − *State Key Laboratory of Coordination Chemistry, MOE Key Laboratory of Mesoscopic Chemistry, MOE Key Laboratory of High Performance Polymer Materials and Technology, Jiangsu Key Laboratory of Green Energy Catalysis and Intelligent Chemical Engineering, Suzhou Key Laboratory of Green Intelligent Manufacturing of New Energy Materials and Devices, Tianchang New Materials and Energy Technologies Research Center, Institute of Green Chemistry and Engineering, School of Chemistry and Chemical Engineering, Nanjing University, Nanjing, Jiangsu 210023, P. R. China*

Complete contact information is available at: https://pubs.acs.org/10.1021/jacs.6c01095

Author Contributions

[#]B.Y., X.L., and S.W. contributed equally to this work.

Notes

The authors declare no competing financial interest.

■ ACKNOWLEDGMENTS

This work was supported by the National Natural Science Foundation of China (U25A20628, 22561160129, 22479074, 22475096), the Equipment Pre-Research and Ministry of Education Joint Fund (8091B02052407), the Fundamental Research Program Key Project of Jiangsu Province (BK20253008), the Science and Technology Major Project of Jiangsu Province (BG2024013), the Scientific and Technological Achievements Transformation Special Fund of Jiangsu Province (BA2023037), the Academic Degree and Postgraduate Education Reforming Project of Jiangsu Province (JGKT24_C001), the Key Core Technology Open Competition Project of Suzhou City (SYG2024122), the Open Research Fund of Suzhou Laboratory (SZLAB-1308-2024-TS005), the Chenzhou National Sustainable Development Agenda Innovation Demonstration Zone Provincial Special Project (2023sfq11, 2025sfq38), and the Fundamental Research Funds for the Central Universities and Nanjing University International Collaboration Initiative (020514380354).

■ REFERENCES

(1) Zhao, C.; Liu, L.; Qi, X.; Lu, Y.; Wu, F.; Zhao, J.; Yu, Y.; Hu, Y.-S.; Chen, L. Solid-State Sodium Batteries. *Adv. Energy Mater.* **2018**, *8* (17), 1703012.

(2) Lu, Y.; Li, L.; Zhang, Q.; Niu, Z.; Chen, J.; Lu, Y.; Li, L.; Zhang, Q.; Niu, Z.; Chen, J. Electrolyte and Interface Engineering for Solid-State Sodium Batteries. *Joule* **2018**, *2* (9), 1747−1770.

(3) Yang, H.; Chen, Y.; Tian, W.; Yuan, S.; Liu, P.; Wang, Q.; Jin, T.; Jiao, L. Co-sustained Release Strategy of Nonflammable Gel Polymer Electrolytes Enables Long-Life Sodium Metal Batteries. *Angew. Chem., Int. Ed.* **2025** *64*, (32), e202506349.

(4) Zhang, H.; Gao, Y.; Liu, X.; Zhou, L.; Li, J.; Xiao, Y.; Peng, J.; Wang, J.; Chou, S. Long-Cycle-Life Cathode Materials for Sodium-Ion Batteries toward Large-Scale Energy Storage Systems. *Adv. Energy Mater.* **2023**, *13* (23), 2300149.

(5) Huang, J.; Wu, K.; Xu, G.; Wu, M.; Dou, S.; Wu, C.; Huang, J.; Wu, K.; Xu, G.; Wu, M.; Dou, S.; Wu, C. Recent Progress and Strategic Perspectives of Inorganic Solid Electrolytes: Fundamentals, Modifications, and Applications in Sodium Metal Batteries. *Chem. Soc. Rev.* **2023**, *52* (15), 4933−4995.

(6) Gao, X.; Xing, Z.; Wang, M.; Nie, C.; Shang, Z.; Bai, Z.; Dou, S. X.; Wang, N.; Zhu, Y.; Yin, J.; Zheng, X.; Emwas, A.-H.; Lei, Y.; Mohammed, O. F.; Cui, Y.; Alshareef, H. N. Comprehensive Insights into Solid-State Electrolytes and Electrode-Electrolyte Interfaces in All-Solid-State Sodium-Ion Batteries. *Energy Storage Mater.* **2023**, *60*, 102821.

(7) Qu, S.; Niu, T.; Qiao, X.; Shen, Y.; Cai, G.; Wang, X.; Wang, Y.; Zhou, Z.; Zhang, S.; Zhang, Z.; Li, G.; Cai, G.; Sun, J. Dual Optimization of Electrolyte and Interface in Na-β''-Al_2O_3 via Ga^{3+} Doping for Advanced Solid-State Sodium Batteries. *Adv. Mater.* **2025**, *37* (41), No. e03562.

(8) Kmiec, S.; Ruoff, E.; Manthiram, A. A New Class of Oxyhalide Solid Electrolytes $NaNbCl_{6-2x}O_x$ for Solid-state Sodium Batteries. *Angew. Chem., Int. Ed.* **2025**, *64* (5), No. e202416979.

(9) Dutra, A. C. C.; Goldmann, B. A.; Islam, M. S.; Dawson, J. A. Understanding Solid-State Battery Electrolytes Using Atomistic Modelling and Machine Learning. *Nat. Rev. Mater.* **2025**, *10*, pages566−583.

(10) Chen, Y.; Qian, J.; Wang, K.; Li, L.; Wu, F.; Chen, R. Cutting-Edge Developments at the Interface of Inorganic Solid-State Electrolytes. *Adv. Mater.* **2025**, *37* (39), 2502653.

(11) Chen, W.; Sun, C. Recent Advances in High Temperature Solid Oxide Electrolytic Cells. *Energy Mater.* **2025**, *5* (5), DOI: 10.20517/energymater.2024.144.

(12) Li, C.; Mu, Y.; Deng, T.; Li, Z.; Lu, G.; Wang, R.; Xu, C. In Situ Construction of a 3D Superionic Skeleton in Sodium Anode for Solid-State Sodium Batteries with a 15 000-Cycle Lifespan at 3C. *Adv. Mater.* **2025**, *37* (20), 2419190.

(13) Logan, S. R.; Wang, T.; Zhang, M.; Zhou, K.; Wang, H.; Shao, A.; Hou, L.; Wang, Z.; Tang, X.; Bai, M.; Li, S.; Ma, Y. A Hetero-Layered, Mechanically Reinforced, Ultra-Lightweight Composite Polymer Electrolyte for Wide-Temperature-Range, Solid-State Sodium Batteries. *Adv. Funct. Mater.* **2023**, *33* (22), 2215117.

(14) Hong, Y.; Jia, K.; Zhang, Y.; Li, Z.; Jia, J.; Chen, J.; Liang, Q.; Sun, H.; Gao, Q.; Zhou, D.; Li, R.; Dong, X.; Fan, X.; He, S. Energetic and Durable All-Polymer Aqueous Battery for Sustainable, Flexible Power. *Nat. Commun.* **2024**, *15* (1), 9539.

(15) Liu, C.; Jia, S.; Yang, T.; Liu, J.; Zhou, X.; Wang, Z.; Dong, H.; Shi, Z.; Zhang, Y.; Chen, Z. Scalable and Ultrathin Dual Entangled

Network Polymer Electrolytes for Safe Solid-State Sodium Batteries. *Angew. Chem., Int. Ed.* **2025**, *64* (26), No. e202505938.
(16) Guo, J.; Feng, F.; Jiang, X.; Wang, R.; Chu, D.; Ren, Y.; Chen, F.; He, P.; Ma, Z.; Chen, S.; Liu, T. Boosting Selective Na^+ Migration Kinetics in Structuring Composite Polymer Electrolyte Realizes Ultrastable All-Solid-State Sodium Batteries. *Angew. Chem., Int. Ed.* **2024**, *34* (26), 2313496.
(17) Bryce, D. L.; Wasylishen, R. E.; Chen, Y.; Qian, J.; Wang, K.; Li, L.; Wu, F.; Chen, R.; Huang, J.; Wu, K.; Xu, G.; Wu, M.; Dou, S.; Wu, C.; Zhao, L.; Hou, M.; Ren, K.; Yang, D.; Li, F.; Yang, X.; Zhou, Y.; Zhang, D.; Liu, S.; Lei, Y.; Liang, F. Hot-Pressing Enhances Mechanical Strength of PEO Solid Polymer Electrolyte for All-Solid-State Sodium Metal Batteries. *Small Methods* **2002**, *8* (10), 2301579.
(18) St-Onge, V.; Rochon, S.; Daigle, J.; Soldera, A.; Claverie, J. P. The Unusual Conductivity of Na^+ in PEO-Based Statistical Copolymer Solid Electrolytes: When Less Means More. *Angew. Chem., Int. Ed.* **2021**, *60* (49), 25897−25904.
(19) Wang, X.; Zhang, C.; Sawczyk, M.; Sun, J.; Yuan, Q.; Chen, F.; Mendes, T. C.; Howlett, P. C.; Fu, C.; Wang, Y.; Tan, X.; Searles, D. J.; Král, P.; Hawker, C. J.; Whittaker, A. K.; Forsyth, M. Ultra-Stable All-Solid-State Sodium Metal Batteries Enabled by Perfluoropolyether-Based Electrolytes. *Nat. Mater.* **2022**, *21* (9), 1057−1065.
(20) Wang, W.; Ding, M.; Chen, S.; Weng, J.; Zhang, P.; Yuan, W.; Bi, A.; Zhou, P. A Novel Composite Solid Electrolyte with Ultrahigh Ion Transference Number and Stability for Solid-State Sodium Metal Batteries. *Chem. Eng. J.* **2024**, *491*, 151989.
(21) An, H.; Li, M.; Liu, Q.; Song, Y.; Deng, B.; Liu, X.; Wang, J. Hybrid Electrolyte Enables Solid-State Sodium Batteries Sustaining 50,000 Cycles. *Angew. Chem., Int. Ed.* **2025**, *8* (6), 661−671.
(22) Liu, K.; Chang, X.; Chen, X.; Liu, X.; Jia, M.; Bi, Z.; Guo, X. Hierarchical-Structural Design of Ultrathin Composite Electrolytes for High-Stability Solid-State Lithium Batteries: From "Polymer-in-Salt" to "Polymer-in-Ceramic.". *Nano Energy* **2025**, *135*, 110644.
(23) Li, X.; Guo, Y.; Wang, Y.; Liu, J.; Wu, Z.; Wang, D. Physicochemical Dual-Force-Driven PVAC@LPSCl Composite Electrolyte Film for High-Performance All-Solid-State Batteries. *Adv. Mater.* **2026**, *36*, No. e12635.
(24) Fu, J.; Wang, C.; Wang, S.; Reid, J. W.; Liang, J.; Luo, J.; Kim, J. T.; Zhao, Y.; Yang, X.; Zhao, F.; Li, W.; Fu, B.; Lin, X.; Hu, Y.; Su, H.; Hao, X.; Gao, Y.; Zhang, S.; Wang, Z.; Liu, J.; Abdolvand, H.; Sham, T.-K.; Mo, Y.; Sun, X. A Cost-Effective All-in-One Halide Material for All-Solid-State Batteries. *Nature* **2025**, *643* (8070), 111−118.
(25) Gao, J.; Tian, S.; Qi, L.; Wang, H.; Yi, B.; Wei, Z.; Yao, S.; Zhao, S.; Gao, Z.; Savilov, S.; Chen, G.; Shen, Z. X.; Du, F. Challenges and Prospectives of Sodium-Containing Solid-State Electrolyte Materials for Rechargeable Metal Batteries. *Mater. Sci. Eng. R Rep.* **2025**, *163*, 100949.
(26) Van Gunsteren, W. F.; Berendsen, H. J. C.; Liu, G.; Yang, J.; Wu, J.; Peng, Z.; Yao, X. Inorganic Sodium Solid Electrolytes: Structure Design, Interface Engineering and Application. *Adv. Mater.* **2024**, *36* (37), 2311475.
(27) Dolomanov, O. V.; Bourhis, L. J.; Gildea, R. J.; Howard, J. A. K.; Puschmann, H. *OLEX2*: A Complete Structure Solution, Refinement and Analysis Program. *J. Appl. Crystallogr.* **2009**, *42* (2), 339−341.
(28) Farrugia, L. J. *WinGX* and *ORTEP for Windows*: An Update. *J. Appl. Crystallogr.* **2012**, *45* (4), 849−854.
(29) Sheldrick, G. M.; Sheldrick, G. M.; Bussi, G.; Donadio, D.; Parrinello, M.; Chiririwa, H.; Meijboom, R.; Krause, L.; Herbst-Irmer, R.; Sheldrick, G. M.; Stalke, D. Comparison of Silver and Molybdenum Microfocus X-Ray Sources for Single-Crystal Structure Determination. *J. Appl. Crystallogr.* **2015**, *48* (1), 3−10.
(30) Sheldrick, G. M.; Sheldrick, G. M.; Bussi, G.; Donadio, D.; Parrinello, M.; Chiririwa, H.; Meijboom, R.; Krause, L.; Herbst-Irmer, R.; Sheldrick, G. M.; Stalke, D. Crystal Structure Refinement with *SHELXL*. *ACTA CRYSTALLOGR A* **2015**, *71* (1), 3−8.
(31) Sheldrick, G. M. *SHELXT*-Integrated Space-Group and Crystal-Structure Determination. *Chem. Phys.* **2015**, *71* (1), 3−8.
(32) Groom, C. R.; Bruno, I. J.; Lightfoot, M. P.; Ward, S. C. The Cambridge Structural Database. *ACTA CRYSTALLOGR B* **2016**, *72* (2), 171−179.
(33) Kratzert, D. *FinalCif, V156* https://dkratzert.de/finalcif.html (accessed 2026−02−10).
(34) Bruker. *SAINT, V8.40B*; Bruker AXS Inc., Madison, WI, USA, 2019.
(35) Chen, Z.; Huang, Z.; Wang, C.; Li, D.; Xiong, Q.; Wang, Y.; Hou, Y.; Wang, Y.; Chen, A.; He, H.; Zhi, C. Supramolecular Crystals Based Fast Single Ion Conductor for Long-Cycling Solid Zinc Batteries. *Angew. Chem. Int. Ed* **2024**, *63* (52), No. e202406683.
(36) Kresse, G.; Joubert, D. From Ultrasoft Pseudopotentials to the Projector Augmented-Wave Method. *Phys. Rev. B* **1999**, *59* (3), 1758−1775.
(37) Grimme, S. Semiempirical GGA-type Density Functional Constructed with a Long-range Dispersion Correction. *J. Comput. Chem.* **2006**, *27* (15), 1787−1799.
(38) Kresse, G.; Furthmuller, J. Effcient Iterative Schemes for Ab Initio Total-Energy Calculations Using a Plane-Wave Basis Set. *Phys. Rev. B* **1996**, *54*, 11169.
(39) Grimme, S.; Antony, J.; Ehrlich, S.; Krieg, H. A Consistent and Accurate *Ab Initio* Parametrization of Density Functional Dispersion Correction (DFT-D) for the 94 Elements H-Pu. *J. Chem. Phys.* **2010**, *132* (15), 154104.
(40) Peljo, P.; Girault, H. H. Electrochemical Potential Window of Battery Electrolytes: The HOMO-LUMO Misconception. *Energy Environ. Sci.* **2018**, *11* (9), 2306−2309.
(41) Van Gunsteren, W. F.; Berendsen, H. J. C.; Liu, G.; Yang, J.; Wu, J.; Peng, Z.; Yao, X. A Leap-Frog Algorithm for Stochastic Dynamics. *Mol. Simul.* **1988**, *1* (3), 173−185.
(42) Essmann, U.; Perera, L.; Berkowitz, M. L.; Darden, T.; Lee, H.; Pedersen, L. G. A Smooth Particle Mesh Ewald Method. *J. Chem. Phys.* **1995**, *103* (19), 8577−8593.
(43) E, W.; Li, D. The Andersen Thermostat in Molecular Dynamics. *Comm. Pure Appl. Math.* **2008**, *61* (1), 96−136.
(44) Bussi, G.; Donadio, D.; Parrinello, M. Canonical Sampling through Velocity Rescaling. *J. Appl. Crystallogr.* **2015**, *67* (1), 3−10.
(45) Akkermans, R. L. C.; Spenley, N. A.; Robertson, S. H. COMPASS III: Automated Fitting Workflows and Extension to Ionic Liquids. *Sci. Adv.* **2021**, *10* (47), 540−551.
(46) Prakash, P.; Fall, B.; Aguirre, J.; Sonnenberg, L. A.; Chinnam, P. R.; Chereddy, S.; Dikin, D. A.; Venkatnathan, A.; Wunder, S. L.; Zdilla, M. J. A Soft Co-Crystalline Solid Electrolyte for Lithium-Ion Batteries. *Nat. Mater.* **2023**, *22* (5), 627−635.
(47) Zhang, S.; Zhao, F.; Chen, J.; Fu, J.; Luo, J.; Alahakoon, S. H.; Chang, L.-Y.; Feng, R.; Shakouri, M.; Liang, J.; Zhao, Y.; Li, X.; He, L.; Huang, Y.; Sham, T.-K.; Sun, X. A Family of Oxychloride Amorphous Solid Electrolytes for Long-Cycling All-Solid-State Lithium Batteries. *Nat. Commun.* **2023**, *14* (1), 3780.
(48) Ling, W.; Mo, F.; Wu, X.; Zeng, X.; Xiong, J.; Huang, Y. Solid-State Eutectic Electrolyte via Solvation Regulation for Voltage-Elevated and Deep-Reversible Zn Batteries. *Nat. Commun.* **2025**, *16* (1), DOI: 10.1038/s41467-025-60125-5.
(49) Tabeta, R.; Aida, M.; Saitô, H. A High-Resolution Solid-State ^{23}Na NMR Study of Sodium Complexes with Solvents, Small Ligand Molecules, and Ionophores. ^{23}Na Chemical Shifts as Means for Identification and Characterization of Ion-Ion, Ion-Solvent, and Ion-Ligand Interactions. *bull. Chem. Soc. Jpn.* **1986**, *59* (6), 1957−1966.
(50) Hernández, G.; Johansson, I. L.; Mathew, A.; Sångeland, C.; Brandell, D.; Mindemark, J. Going Beyond Sweep Voltammetry: Alternative Approaches in Search of the Elusive Electrochemical Stability of Polymer Electrolytes. *J. Electrochem. Soc.* **2021**, *168* (10), 100523.
(51) Zhou, L.; Zhang, S.; Li, W.; Li, B.; Grundish, N. S.; Ren, P.; Wang, X.; Wu, N.; Zhou, W.; Li, Y.; Li, C.; Mu, Y.; Deng, T.; Li, Z.; Lu, G.; Wang, R.; Xu, C.; Li, X.; Guo, Y.; Wang, Y.; Liu, J.; Wu, Z.; Wang, D. Amorphous-Nanocrystalline Fluorinated Halide Electrolytes with High Ionic Conductivity and High-Voltage Stability. *J. Am. Chem. Soc.* **2025**, *147* (18), 15136−15145.

(52) Logan, S. R. The Origin and Status of the Arrhenius Equation. *Adv. Funct. Mater.* **1982**, *59* (4), 279.
(53) Han, F.; Westover, A. S.; Yue, J.; Fan, X.; Wang, F.; Chi, M.; Leonard, D. N.; Dudney, N. J.; Wang, H.; Wang, C. High Electronic Conductivity as the Origin of Lithium Dendrite Formation within Solid Electrolytes. *Nat. Energy* **2019**, *4* (3), 187−196.
(54) Tseng, K.-T.; Lee, K.; Sakamoto, J.; An, H.; Li, M.; Liu, Q.; Song, Y.; Deng, B.; Liu, X.; Wang, J.; Guo, J.; Feng, F.; Jiang, X.; Wang, R.; Chu, D.; Ren, Y.; Chen, F.; He, P.; Ma, Z.; Chen, S.; Liu, T.; Chen, W.; Sun, C.; Kmiec, S.; Ruoff, E.; Manthiram, A. Enabling "Sodium-Metal-Free" Manufacturing of Solid-State Batteries. *ACS Energy Lett.* **2024**, *9* (9), 4544−4549.
(55) Gao, J.; Tian, S.; Qi, L.; Wang, H. Intercalation Manners of Perchlorate Anion into Graphite Electrode from Organic Solutions. *Mater. Sci. Eng. R Rep.* **2015**, *176*, 22−27.
(56) Gao, X.; Xing, Z.; Wang, M.; Nie, C.; Shang, Z.; Bai, Z.; Dou, S. X.; Wang, N.; Zhu, Y.; Yin, J.; Zheng, X.; Emwas, A.-H.; Lei, Y.; Mohammed, O. F.; Cui, Y.; Alshareef, H. N. Concentrated Dual-Cation Electrolyte Strategy for Aqueous Zinc-Ion Batteries. *Energy Environ. Sci.* **2023**, *14* (8), 4463−4473.
(57) Younesi, R.; Christiansen, A. S.; Scipioni, R.; Ngo, D.-T.; Simonsen, S. B.; Edström, K.; Hjelm, J.; Norby, P. Analysis of the Interphase on Carbon Black Formed in High Voltage Batteries. *J. Electrochem. Soc.* **2015**, *162* (7), A1289−A1296.

https://doi.org/10.1021/jacs.6c01095
J. Am. Chem. Soc. 2026, 148, 21588−21598